



Morphological instability and roughening of growing 3D bacterial colonies

Alejandro Martínez-Calvo^{a,b,1}, Tapomoy Bhattacharjee^{c,1,2}, R. Konane Bay^{b,3}, Hao Nghi Luu^b, Anna M. Hancock^b, Ned S. Wingreen^{a,d,e,4}, and Sujit S. Datta^{b,4}

Edited by Herbert Levine, Northeastern University, Boston, MA; received May 11, 2022; accepted September 16, 2022

How do growing bacterial colonies get their shapes? While colony morphogenesis is well studied in two dimensions, many bacteria grow as large colonies in three-dimensional (3D) environments, such as gels and tissues in the body or subsurface soils and sediments. Here, we describe the morphodynamics of large colonies of bacteria growing in three dimensions. Using experiments in transparent 3D granular hydrogel matrices, we show that dense colonies of four different species of bacteria generically become morphologically unstable and roughen as they consume nutrients and grow beyond a critical size—eventually adopting a characteristic branched, broccoli-like morphology independent of variations in the cell type and environmental conditions. This behavior reflects a key difference between two-dimensional (2D) and 3D colonies; while a 2D colony may access the nutrients needed for growth from the third dimension, a 3D colony inevitably becomes nutrient limited in its interior, driving a transition to unstable growth at its surface. We elucidate the onset of the instability using linear stability analysis and numerical simulations of a continuum model that treats the colony as an “active fluid” whose dynamics are driven by nutrient-dependent cellular growth. We find that when all dimensions of the colony substantially exceed the nutrient penetration length, nutrient-limited growth drives a 3D morphological instability that recapitulates essential features of the experimental observations. Our work thus provides a framework to predict and control the organization of growing colonies—as well as other forms of growing active matter, such as tumors and engineered living materials—in 3D environments.

bacteria | living matter | morphogenesis | growth instability

Bacteria are known to thrive in diverse ecosystems and habitats (1–4). In nature, bacteria can be found growing on surfaces, which in addition to the ease of visualization in two dimensions, have led laboratory studies to typically focus on colony growth on two-dimensional (2D) planar surfaces. However, in many cases in nature, bacteria grow in three-dimensional (3D) habitats, such as gels and tissues inside of hosts (5–7), soils and other subsurface media (8, 9), wastewater treatment devices, and naturally occurring bodies of water (10–12). Nonetheless, despite their prevalence, the morphodynamics of bacterial colonies growing in such 3D environments remains largely unknown. Here, we ask: what determines the shape of a bacterial colony growing in three dimensions? And are there general characteristics and universal principles that span across species and specific environmental conditions?

Studies of bacteria growing on 2D planar surfaces have revealed a variety of growth patterns, ranging from circular-shaped colonies (13–19) to herringbone patterns (20) and ramified, rough interfaces (13–18, 21). Some of these patterns become 3D as the colony can grow and deform into the third dimension. These morphologies are now understood to arise from friction between the growing colony and the surface and differential access to nutrients, which may also be available from the third dimension (13–18, 20, 22–26). The emergent patterns have been rationalized by incorporating these key ingredients into reaction–diffusion equations (14–16, 18, 22, 27–36), active continuum theories (19–21, 28, 31, 37–53), and agent-based models (28, 31, 38, 40, 45, 46, 54–57). Moreover, it has been suggested that these growth patterns may, in turn, influence the global function and physiology of bacterial colonies (58–60), including resistance to antibiotics (61–63) and parasites (64), resilience to environmental changes (65, 66), and genetic diversity (56, 58, 59, 67–73). However, in stark contrast to the considerable scientific effort devoted to studying 2D growth, little is known about the collective processes, the resulting morphologies, or their functional consequences for bacteria growing in three dimensions.

From a physics standpoint, growing in three dimensions is fundamentally different from growing in two dimensions in terms of both nutrient access and the ability to grow and deform into an additional dimension. Consequently, we expect colony

Significance

The morphogenesis of two-dimensional bacterial colonies has been well studied. However, little is known about the colony morphologies of bacteria growing in three dimensions, despite the prevalence of three-dimensional environments (e.g., soil, inside hosts) as natural bacterial habitats. Using experiments on bacteria in granular hydrogel matrices, we find that dense multicellular colonies growing in three dimensions undergo a common morphological instability and roughen, adopting a characteristic broccoli-like morphology when they exceed a critical size. Analysis of a continuum “active fluid” model of the expanding colony reveals that this behavior originates from an interplay of competition for nutrients with growth-driven colony expansion, both of which vary spatially. These results shed light on the fundamental biophysical principles underlying growth in three dimensions.

The authors declare no competing interest.

This article is a PNAS Direct Submission.

Copyright © 2022 the Author(s). Published by PNAS. This open access article is distributed under Creative Commons Attribution-NonCommercial-NoDerivatives License 4.0 (CC BY-NC-ND).

¹A.M.-C. and T.B. contributed equally to this work.

²Present address: National Centre for Biological Sciences, Tata Institute of Fundamental Research, Bangalore 560065, India.

³Present address: Department of Chemical and Biological Engineering, University of Colorado Boulder, Boulder, CO 80309.

⁴To whom correspondence may be addressed. Email: wingreen@princeton.edu or ssdatta@princeton.edu.

This article contains supporting information online at <https://www.pnas.org/lookup/suppl/doi:10.1073/pnas.2208019119/-DCSupplemental>.

Published October 18, 2022.

morphodynamics—the way a colony's overall shape changes over time—to also be different. Some recent studies hint that this is indeed the case, showing how specific mechanical interactions imposed by a 3D environment can influence the morphology of growing biofilms. For instance, external fluid flows are now known to trigger the formation of streamers that stem from an initially surface-attached colony (10, 74). Also, under quiescent conditions, small (at most tens of cells across) biofilm colonies constrained in cross-linked gels adopt internally ordered structures as they grow and push outward (75), mediated by elastic stresses arising at the interface between the colony and its stiff environment. However, the behavior of larger bacterial colonies growing freely in quiescent 3D environments remains underexplored, despite the fact that they represent a fundamental building block of more complex natural colonies.

Here, we combine experiments, theoretical modeling, and numerical simulations to unravel the morphodynamics of large colonies growing in 3D environments. By performing experiments with four different species of bacteria growing in transparent and easily deformed granular hydrogel matrices, we find that dense colonies growing in three dimensions undergo a morphological instability and roughen when they become nutrient limited in their interior. Independent of variations in cell type and environmental conditions, growing colonies eventually adopt a generic highly branched, broccoli-like morphology with a characteristic roughness exponent and power spectrum. Employing a continuum “active fluid” model that incorporates the coupling between nutrient diffusion, consumption, and cell growth, we trace the origin of the instability to an interplay of competition for nutrients with growth pressure–driven colony expansion. In particular, we find that these dense 3D colonies inevitably become nutrient limited in their interior, which eventually drives the periphery of the colony to become unstable and roughen. Our results thus help establish a framework to predict and control the organization of growing colonies in 3D habitats. These principles could also extend to other morphogenesis processes driven by growth in 3D environments, such as developmental processes (76, 77), tumor growth (78–82), and the expansion of engineered soft living materials (83, 84).

Results

Growing 3D Bacterial Colonies Undergo a Common Morphological Instability and Roughening. To explore the morphodynamics of dense bacterial colonies growing in 3D environments, we use a bioprinter to inject densely packed (number density $\rho \sim 10^{12}$ cells mL^{-1}) colonies of bacteria inside granular hydrogel matrices, as sketched in Fig. 1A ([SI Appendix](#)). To start, we focus on experiments using *Escherichia coli* as a model system. The colonies have long cylindrical shapes with radii R that vary between ~ 20 and $250 \mu\text{m}$, at least tens of cells across. The matrices have four notable characteristics (33, 85–87). (I) They are transparent, enabling us to directly visualize colony morphodynamics *in situ*. (II) They are easily mechanically deformed and rearranged (yielded), and thus, they do not strongly constrain colony growth but simply keep the cells suspended in 3D, unlike in previous work (75). (III) They can be designed to be replete with oxygen and nutrients given that the internal mesh size of the individual hydrogel grains is ~ 40 to 100 nm (88) and thus, permissive of free diffusion of small molecules throughout each matrix, thereby sustaining cellular proliferation over many generations. (IV) The sizes of the interstitial pores between adjacent hydrogel grains can be precisely tuned by changing the hydrogel grain packing density (33, 88). To isolate the influence of cellular growth on

colony morphodynamics, we use hydrogel matrices with mean pore sizes between ≈ 0.1 and $1.0 \mu\text{m}$ (i.e., smaller or comparable with the diameter of a single cell). Hence, the bacteria are stuck inside the pores; even if they are nominally motile, they cannot self-propel through the pore space. Nevertheless, as the cells consume nutrients, they grow—transiently deforming and yielding the surrounding matrix—and push their progeny out into the neighboring available pores ([Movies S1](#) and [S2](#)).

It was recently shown that colonies of motile *E. coli* in similar matrices but with pores sufficiently large for cells to swim through smooth out any perturbations to their colony morphology using directed motility (34, 35). We observe starkly differing behavior for the case of the purely growth-driven colony expansion considered here. When the matrix pore size is small enough to abolish the influence of motility, a growing colony of *E. coli* instead exhibits a striking morphological instability and eventually roughens—adopting a highly branched, broccoli-like interface, as shown by the example in Fig. 1B and [Movie S3](#). The cells constitutively express green fluorescent protein (GFP) in their cytoplasms, which enables us to directly visualize the colony morphodynamics in 3D across scales spanning from the width of a single cell to that of the entire colony using confocal microscopy; Fig. 1B shows bottom-up projections of the cellular fluorescence intensity measured using a 3D stack of confocal micrographs, with successive planar slices taken at different depths within the colony. This growth-induced instability and roughening are markedly different from that observed in ref. 75, where much smaller bacterial colonies growing as inclusions in stiff, cross-linked bulk gels retained smooth surfaces. Moreover, while highly branched shapes have been previously observed for colonies growing on planar 2D surfaces, they are thought to only arise when the underlying surface is depleted in nutrients, thereby generating stochasticity in the ability of cells to access nutrients (13–18, 22, 23, 37); in our case, however, the surrounding matrix is nutrient replete.

To characterize the colony shape, we track its one-dimensional (1D) leading edge over time, as shown in Fig. 1C. The rough colony surface exhibits fluctuations in the axial direction z over a broad range of length scales, ranging from the size of a single cell to hundreds of cells. However, these fluctuations appear to have a characteristic maximal size ~ 100 to $200 \mu\text{m}$, as shown by the “florets”—to use the analogy of broccoli—in Fig. 1B and C. For clarity of terminology, we refer to the development of the characteristic large-scale floret size and the development of the smaller-scale fluctuations separately as the “morphological instability” and “roughening,” respectively. These features can be quantified using the power spectral density of spatial fluctuations, $S(k, t) = \left| L^{-1} \int_0^L dz [R(z, t) - \bar{R}(t)] \exp(-ikz) \right|^2$, as shown in Fig. 1D at time $t = 37 \text{ h}$; here, \bar{R} is the average radius of the leading edge, $k = 2\pi/\lambda$ is the axial wave number corresponding to a wavelength λ , and L is the length of the analyzed region of the colony along the axial direction z . In particular, $S(k)$ eventually becomes time independent ([SI Appendix](#), Fig. S1) and exhibits an apparent power-law decay $\sim k^{-\nu}$ with $\nu \approx 2.3$ at sufficiently small length scales (large k), as indicated by the dashed line in Fig. 1D, which implies that the spatial fluctuations of the rough colony surface have a fractal structure over multiple scales—although further studies over a broader range of large k are needed to rigorously establish this fractal nature and the corresponding power-law scaling exponent. By contrast, $S(k)$ becomes bounded at sufficiently large length scales (small k), as indicated in Fig. 1D. Indeed, we again find that the majority of the power is confined to wave numbers corresponding to a characteristic wavelength $\lambda_{\text{exp}}^* \sim 100$ to $200 \mu\text{m}$ —as highlighted by the complementary

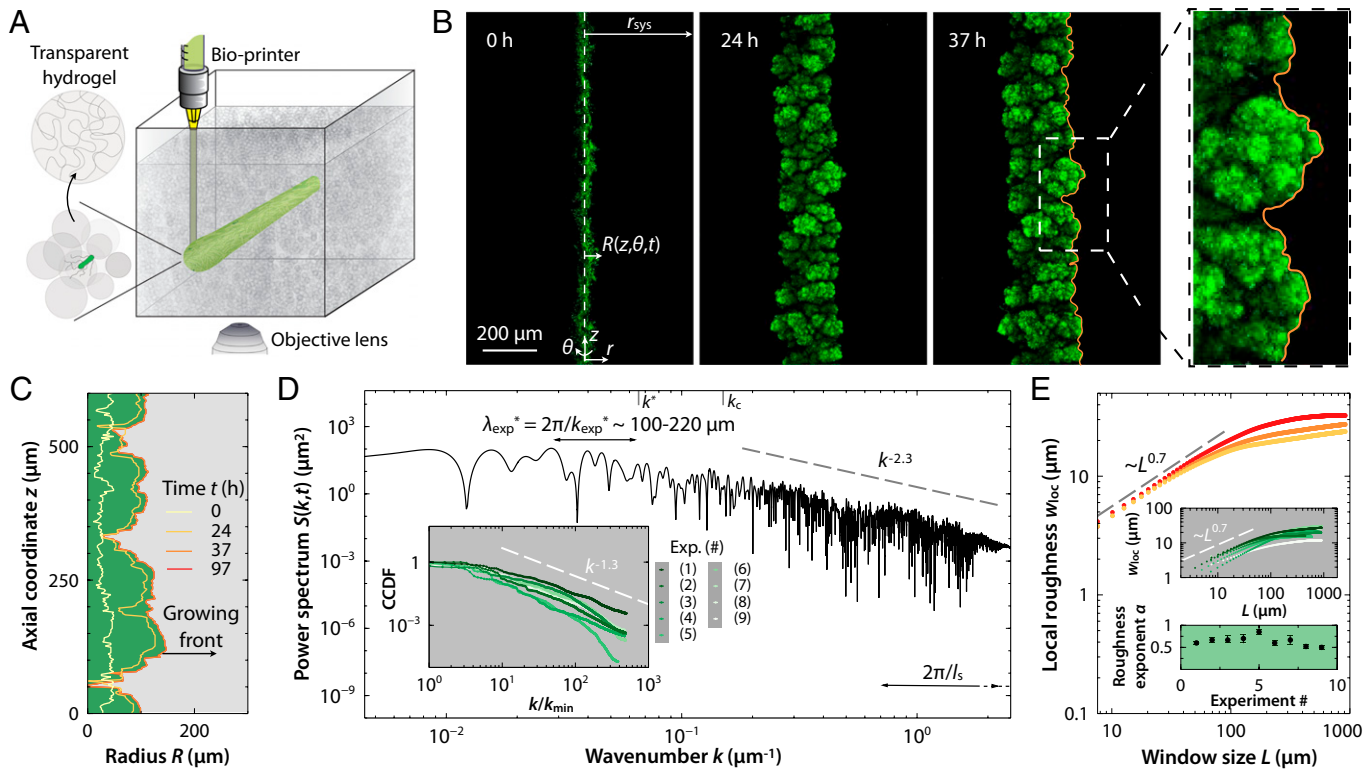


Fig. 1. Dense bacterial colonies become morphologically unstable and roughen as they grow in three dimensions. (A) Schematic of the experiments in which a dense bacterial colony (green cylinder) is 3D printed within a transparent matrix made of jammed hydrogel grains (gray). The matrix locally yields as cells are injected into the pore space, and then, it rapidly rejams around the dense-packed cells, holding them in place. The individual hydrogel grains are highly swollen in liquid media containing salts and nutrients, which can freely pass through. However, the interstitial pores between grains are smaller than the cell body size, thereby suppressing any motility and holding the cells in place; the colony then expands outward solely through cellular growth and division into adjacent available pores. We use confocal microscopy to obtain 3D stacks of optical slices of cell body fluorescence at different depths in the medium. (B) Snapshots of the time evolution of a colony of *E. coli* displaying morphological instability and roughening as the colony grows. The rightmost panel displays a magnified view of the colony shown at 37 h. The images show maximum-intensity projections of the confocal optical slices taken at different depths in the medium. (C) Profiles of the leading edge of the colony shown in B at the same times as in B. (D) Power spectrum $S(k, t)$ of the leading edge of the colony in B at time $t = 37$ h as a function of the axial (along z) wave number k . The lower and upper limits of the wave numbers displayed correspond to the size of the domain and the experimental resolution limit, respectively. The double-headed arrow indicates the characteristic wavelength of the large-scale fluctuations in the shape of the colony surface measured experimentally, λ_{exp}^* , corresponding to a wave number $k_{\text{exp}}^* = 2\pi/\lambda_{\text{exp}}^*$. The gray ticks indicate the most-unstable and cutoff wave numbers predicted by our linear stability analysis, k^* and k_c , respectively, using a substrate penetration length $l_s = 5 \mu\text{m}$ (with the range of estimated $2\pi/l_s$ also indicated in the lower right) as described in SI Appendix. (D, Inset) CCDF of the power spectra of different experiments for *E. coli* colonies testing different strains, matrix stiffnesses and pore sizes, and nutrient concentrations, as summarized in SI Appendix, Table S2; k_{min} is the wave number corresponding to the domain size that we use to normalize the different CCDFs. We observe similar power-law scaling, with a plateau at small k , in all cases. (E) Local roughness w_{loc} as a function of the observation window size L for the experiment shown in B at times $t = 24, 37$, and 97 h. (E, Insets) Local roughness w_{loc} as a function of L (E, Upper Inset) and the corresponding roughness exponent α (E, Lower Inset) for the same experiments shown in D, Inset at the same times.

cumulative distribution function (CCDF) of the power spectrum shown in Fig. 1 D, Inset.

We further characterize the colony surface roughening by computing the local roughness of the leading edge quantified by the local variance of the colony radius, $w_{\text{loc}}^2(L, t) = \langle [R(z, t) - \bar{R}_L(t)]^2 \rangle_L$, where $\langle \cdot \rangle_L$ denotes the spatial average over different windows of size L along the axial direction z and $\bar{R}_L(t)$ is the average radius in this window. We find that the local roughness of the leading edge appears to scale as $w_{\text{loc}} \sim L^\alpha$ up to a window size comparable with the characteristic wavelength $\lambda_{\text{exp}}^* \sim 100$ to $200 \mu\text{m}$, above which w_{loc} saturates (Fig. 1E). The so-called roughness exponent $\alpha \approx 0.7$, as shown by the dashed line, corresponding to a fractal dimension $d_f = 2 - \alpha \approx 1.3$ (89). Indeed, the power-law decay of the power spectrum $S(k)$ and this roughness exponent agree well with the relation expected from the celebrated Family–Vicsek dynamic scaling of fractal interfaces in one dimension, namely that $\nu = 1 + 2\alpha$ (89, 90)—confirming that over length scales smaller than the characteristic floret size $\lambda_{\text{exp}}^* \sim 100$ to $200 \mu\text{m}$, the colony surface appears to be fractal like.

To investigate the generality of these morphodynamics, we perform replicates of this same experiment, exploring a broad

range of different cell types and environmental conditions (SI Appendix, Figs. S1–S14 and Table S2). Remarkably, we find similar colony instability and roughening that arises within just a few hours (i.e., comparable with the doubling time of the cells) in all cases. Growing colonies of cells that are either motile or nonmotile in unconfined liquid but are too confined to be motile in the hydrogel matrices shows similar morphodynamics (SI Appendix, Figs. S1, S2, S4–S6, and S9)—confirming that the instability and roughening are driven solely by cellular growth and division. For this case of growth-driven colony expansion, we also observe similar overall features of morphological instability and roughening independent of the hydrogel matrix pore size and deformability (SI Appendix, Figs. S1–S6 and S9–S14)—suggesting that these morphodynamics are not strongly sensitive to specific granular features of or mechanical interactions with the surrounding matrix. Finally, we also find a similar instability and roughening for colonies in matrices with differing nutrient characteristics and concentrations, with differing initial radii, and importantly, across different strains of either *E. coli* or the biofilm formers *Vibrio cholerae*, *Pseudomonas aeruginosa*, and *Komagataeibacter sucrofermentans* (SI Appendix,

Figs. S1–S14 and S24)—indicating that this morphological instability is not a manifestation of a specific nutrient environment or cell type. Taken together, these results establish that large, dense bacterial colonies growing freely in three dimensions generically become morphologically unstable and roughen, adopting the same characteristic broccoli-like morphology (Fig. 1 *D*, *Inset* and *E*, *Insets*) that is fractal like at small length scales, and bounded at larger length scales by a characteristic floret size spanning hundreds of cells across.

The Interiors of Large, Dense Colonies Are Depleted of a Substrate Essential for Growth, Causing a Morphological Instability and Surface Roughening. What causes colony instability and roughening? Close inspection of the micrographs for the experiment in Fig. 1 provides a clue; we find that cells only $\lesssim 20 \mu\text{m}$ from the colony surface are fluorescent, while those deeper inside the colony lose fluorescence, as shown in *SI Appendix*, Fig. S15. Because the GFP fluorescence acts as a proxy indicator for metabolically active cells, and because cellular metabolism of carbon-containing nutrients is both nutrient and oxygen dependent, this observation suggests that colony growth is limited to this small surface layer.

This suggestion is corroborated by a balance of either nutrient or oxygen 1D diffusion into the cylindrical colony with consumption by the cells (*SI Appendix*), which suggests that they penetrate into the colony over a length scale $l_n = \sqrt{D_n c_{\text{half},n} / (k_n \rho)}$ or $l_{O_2} = \sqrt{D_{O_2} c_{\text{half},O_2} / (k_{O_2} \rho)}$, where ρ is cell density; D_n , D_{O_2} are the diffusivities; k_n , k_{O_2} are the maximal uptake rates per cell; and $c_{\text{half},n}$, c_{half,O_2} are characteristic Michaelis–Menten concentrations of nutrient or oxygen. In particular, using parameter values representative of our experiments (*SI Appendix*, Table S1) yields $l_n \approx 1$ to $9 \mu\text{m}$ and $l_{O_2} \approx 5 \mu\text{m}$, comparable with the length scale over which fluorescence persists. (Because both l_n and l_{O_2} are comparable with each other for all our experiments, hereafter, we will use the subscript “*s*” and the term substrate for whichever limits cellular growth and division; indeed, the theoretical results that follow are not noticeably altered when considering nutrient vs. oxygen as the limiting substrate, as detailed in *SI Appendix* and Fig. S16.) Thus, for a large and dense 3D bacterial colony, growth is localized to just a few layers of cells at the colony surface, with either nutrient or oxygen acting as a limiting substrate. Consequently, we expect that the relative strength of random fluctuations in cellular growth and division along the colony surface is amplified, potentially driving morphological instability and roughening in a manner similar to 2D colonies (28, 31, 32, 55, 91–93).

As a final test of this hypothesis, we repeat our experiments but now with each colony initially inoculated on the planar surface atop a granular hydrogel matrix, exposed to humid air above—just as in conventional studies of growth on 2D gels. In this case, the colony can either grow laterally in two dimensions on the surface, accessing nutrients and oxygen from the third dimension akin to purely 2D colonies, or it can grow into the 3D matrix below, becoming substrate limited in its interior akin to purely 3D colonies. Thus, when the hydrogel matrix is nutrient replete, we expect that all cells in the colony on the surface of the matrix remain metabolically active and fluorescent, and the lateral colony edge remains smooth, as expected for purely 2D colonies that are not nutrient depleted (13–19); by contrast, the cells that grow into the underlying matrix should eventually lose fluorescence, and the corresponding colony surface will become unstable and roughen, similar to purely 3D colonies. These expectations are indeed borne out by the experiments, as shown in *SI Appendix*, Figs. S17 and S18. Thus, unlike 2D colonies that

can use growth substrates that are available from the third dimension, dense colonies growing in 3D environments inevitably become substrate limited in their interiors—causing growth to be localized at their surfaces, amplifying inherent random fluctuations in growth along the surface, and thereby, generating morphological instability and roughening.

Continuum Model of a Growing 3D Bacterial Colony. To rationalize the experimental observations and test our hypothesis regarding the morphological instability and roughening, we model a densely packed growing bacterial colony embedded in a 3D hydrogel by means of a continuum theory, where bacteria are treated as an active fluid whose expansion is driven by substrate-dependent growth; here, we use the term “active” to reflect the process of cellular growth. Similar approaches were used to model growing bacterial colonies in other settings (28, 31, 32, 37, 39, 50, 73) as well as other biological morphodynamics (94–100). In Fig. 2*A*, the model is schematized for a slab geometry, which can represent a small region of the surface of a cylindrical colony. In our approach, the colony is described in terms of a substrate concentration field $c(\mathbf{x}, t)$, a velocity field $\mathbf{u}(\mathbf{x}, t)$, and a growth pressure field inside the colony $p(\mathbf{x}, t)$, where \mathbf{x} and t denote positional coordinate and time, respectively. Because the bacteria inside the colony are effectively incompressible and close packed, we assume a constant cellular density $\rho \sim 10^{12} \text{ cells mL}^{-1}$ and assume that the velocity field in the interior of the growing colony obeys Darcy’s law, with local velocity proportional to local pressure gradient ∇p , which yields a curl-free velocity field.

We consider both a slab geometry to best elucidate the relevant physics and a cylindrical geometry to directly compare with the experiments (*SI Appendix*). We therefore adopt Cartesian and cylindrical coordinates, respectively, to describe the evolution of the growing colony, whose surface is located at $x = X(y, z, t)$ for a slab-shaped colony (Fig. 2*A*) and at $r = R(z, \theta, t)$ for a cylindrical colony (Fig. 1*B*). The mass, momentum, and substrate conservation equations are

$$\left. \begin{array}{l} \text{Bacterial growth : } \nabla \cdot \mathbf{u} = gf(c_{\text{in}}) \\ \text{Darcy flow : } -\nabla p - \xi \mathbf{u} = \mathbf{0} \\ \text{Substrate diffusion and uptake : } \partial_t c_{\text{in}} = D_s \nabla^2 c_{\text{in}} - k_s \rho f(c_{\text{in}}) \end{array} \right\} \text{for } \begin{cases} 0 \leq x \leq X : \text{Slab}, \\ 0 \leq r \leq R : \text{Cylinder}, \end{cases} \quad [1\mathbf{a}]$$

and they are coupled to substrate diffusion outside the colony:

$$\partial_t c_{\text{out}} = D_s \nabla^2 c_{\text{out}} \text{ for } \begin{cases} X \leq x \leq x_{\text{sys}} : \text{Slab}, \\ R \leq r \leq r_{\text{sys}} : \text{Cylinder}, \end{cases} \quad [1\mathbf{b}]$$

where $\mathbf{x} = (x, y, z)$, $\mathbf{u} = (u_x, u_y, u_z)$ for a slab-shaped colony and $\mathbf{x} = (z, r, \theta)$, $\mathbf{u} = (u_z, u_r, u_\theta)$ for a cylindrical colony. Here, g is the maximal bacterial growth rate; $c_{\text{in}}(\mathbf{x}, t)$ and $c_{\text{out}}(\mathbf{x}, t)$ denote the substrate concentration inside and outside the colony, respectively; $f(c_{\text{in}}) = c_{\text{in}} / (c_{\text{half},s} + c_{\text{in}})$ is the Michaelis–Menten function reflecting the substrate dependence of consumption relative to the characteristic concentration $c_{\text{half},s}$ (101, 102); and ξ is an effective cell-matrix friction coefficient that relates the gradient in growth pressure to the speed of expansion. Additionally, x_{sys} and r_{sys} describing the size of the overall system are given by the outermost width and radius of the hydrogel matrix, respectively.

As boundary conditions, we impose surface stress balance, substrate continuity, and the kinematic condition (i.e., $\partial_t \mathbf{x}_{\text{surf}} \cdot \mathbf{n} = \mathbf{u} \cdot \mathbf{n}$), which relate the front velocity and the local velocity of the colony at the moving front, $x = X(y, z, t)$ and $r = R(z, \theta, t)$, where \mathbf{x}_{surf} and \mathbf{n} are the parametrization and the unit normal

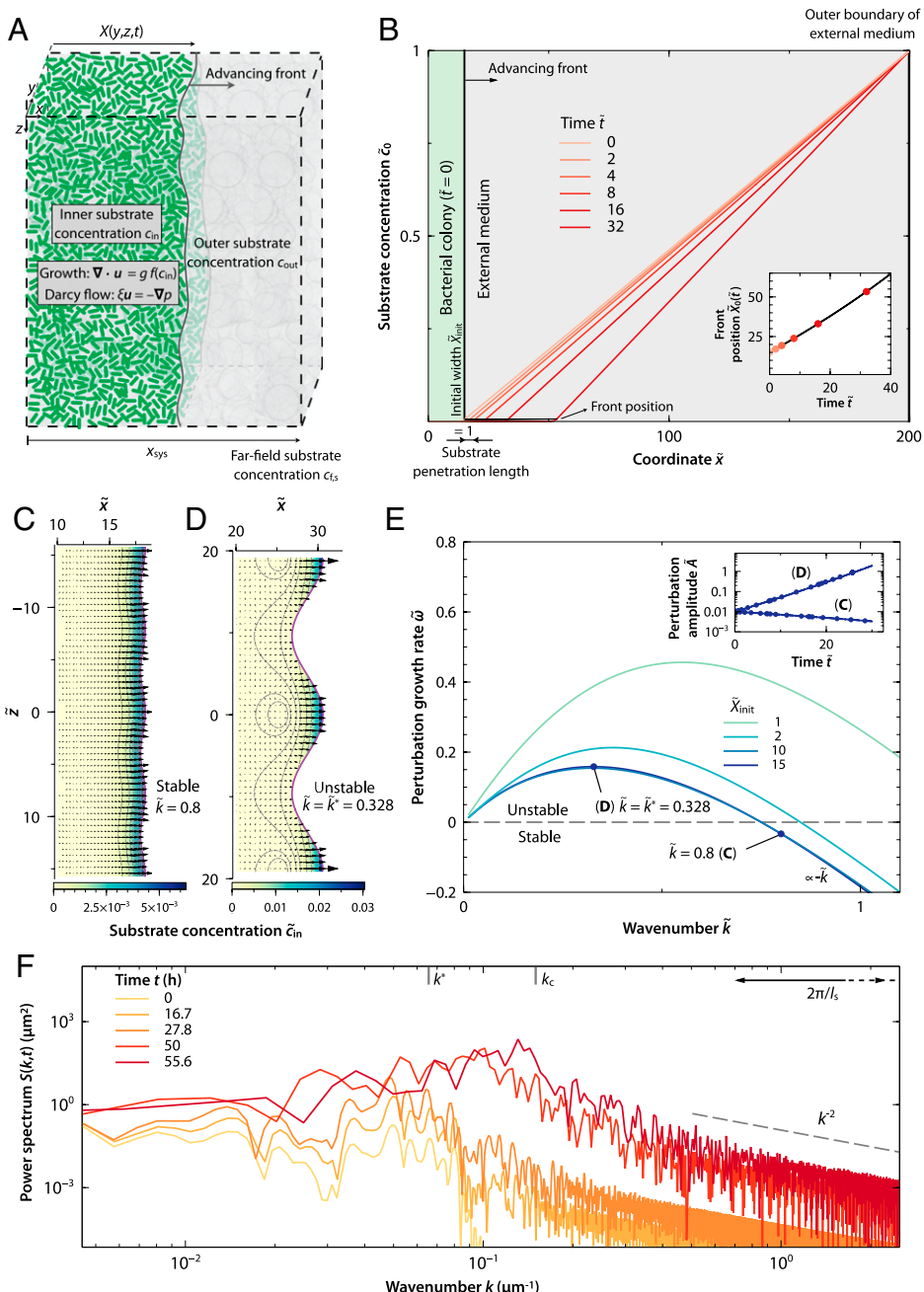


Fig. 2. A minimal continuum model suggests that colonies growing in three dimensions are intrinsically unstable. (A) Schematic of the model, in which we treat a slab-shaped bacterial colony (green) as an active fluid that expands along the x coordinate due to the pressure generated by growth mediated by substrate availability and consumption. The model is 2D (i.e., taken to be uniform and infinite along the y coordinate). (B) Dimensionless substrate concentration as a function of position \tilde{x} at different times, displaying both the inner and outer solutions, \tilde{c}_{in} and \tilde{c}_{out} , for an initial dimensionless colony width $\tilde{X}_{init} = 15$ and system width $\tilde{x}_{sys} = 200$ for the case where the front has been forced to be flat. The substrate penetrates only a small distance into the colony before it is completely consumed, and thus, growth is localized to a thin surface layer. (B, Inset) Evolution of the advancing planar front $\tilde{X}_0(\tilde{t})$ as a function of time as given by the 1D planar kinematic condition, $d\tilde{X}_0/d\tilde{t} = \tilde{u}_0(\tilde{X}_0) \cdot e_x$ (*SI Appendix*, Eq. S10); points show specific times, while the black curve shows the numerical solution for all times. (C and D) Color plots of the dimensionless substrate concentration inside the bacterial colony \tilde{c}_{in} , the cellular velocity vector field \tilde{u} (arrows), and contours of the growth pressure field \tilde{p} for an initially sinusoidally perturbed colony surface with (C) a stable wave number, $\tilde{k} = 0.8$, at time $\tilde{t} = 2.9$ and (D) the same but for a perturbation with the most-unstable wave number, $\tilde{k} = \tilde{k}^* = 0.328$ at time $\tilde{t} = 12.3$. Both cases are obtained for an initial colony width $\tilde{X}_{init} = 15$, system width $\tilde{x}_{sys} = 200$ (same as in B), and initial perturbation amplitude $\tilde{\epsilon} = 0.01$. (E) Perturbation growth rate $\tilde{\omega}$ as a function of wave number \tilde{k} for the slab geometry with $\tilde{x}_{sys} = 200$ and different values of the initial colony width \tilde{X}_{init} . The dots correspond to the wave numbers of the fronts shown in C and D. (E, Inset) Perturbation amplitude $\tilde{\Lambda}$ as a function of time \tilde{t} obtained from linear stability analysis (solid lines) and full numerical simulations (dots) for the two cases in C and D. (F) Power spectrum $S(k,t)$ as a function of the wave number k at different times (indicated by the different colors in the legend) obtained from full numerical simulations of Eq. 1, with $\tilde{X}_{init} = 50$, $\tilde{x}_{sys} = 400$, $\Gamma = 0$, and a front initially perturbed with white noise of amplitude $\tilde{\epsilon} = 0.01$ up to $\tilde{k} = 0.4$, with a domain length of $\tilde{L} = 320$ and a characteristic timescale $t_c = 2.2$ h. The gray ticks indicate the most-unstable and cutoff wave numbers predicted by our linear stability analysis, k^* and k_c , respectively, using a substrate penetration length $l_s = 5$ μm (with the range of estimated $2\pi/l_s$ also indicated in the lower right) as described in *SI Appendix*.

vector of the moving surface, respectively. We also impose a constant substrate concentration, $c_{f,s}$, at the outermost system boundary, $x = x_{sys}$ and $r = r_{sys}$.

Parameters Characterizing 3D Colony Growth. To distill the relevant physics from our theoretical model, we first reduce the number of parameters in Eq. 1 by employing dimensional

analysis and selecting appropriate quantities to scale the system of equations—as detailed further in *SI Appendix*.

First, given that colony growth is a slow process (e.g., Fig. 1*B*), we assume that the spatial profile of substrate rapidly adjusts to any change in the colony due to growth. We verify the validity of this assumption *a posteriori* (*SI Appendix*). Moreover, as discussed, because substrate uptake is much faster than substrate diffusion at the scale of the overall colony (*SI Appendix*, Table S1), $c_{\text{in}} \sim 0$ inside the colony. Thus, there are two distinct regions in the colony: the substrate-depleted interior and an actively growing boundary layer at the colony surface whose thickness is much smaller than R . In this surface layer, substrate diffusion and uptake are always in quasisteady-state balance—again yielding the substrate penetration length into the colony $l_s = \sqrt{D_s c_{\text{half},s} / (k_s \rho)}$ introduced earlier. This penetration length sets the characteristic length scale $l_c = l_s$. We expect that $c_{\text{in}} \ll c_{\text{f},s}$, $c_{\text{half},s}$ inside this boundary layer, as the substrate source is far from the colony surface in the experiments (i.e., $r_{\text{sys}} \gg R$). Therefore, in what follows, we consider the limit $c_{\text{in}} \ll c_{\text{half},s}$, where the Michaelis-Menten function simplifies to $f(c_{\text{in}}) \simeq c_{\text{in}} / c_{\text{half},s}$.

As the main mechanism driving the expansion of the bacterial colony is growth mediated by substrate consumption, the characteristic scales for time t_c and front velocity u_c are obtained from the balance between mass conservation and bacterial growth in Eq. 1*a*, as well as the kinematic condition of the front, which sets $u_c = l_s / t_c$. The natural timescale t_c is the inverse of the mean growth rate of cells within the growing front. In the substrate-limited regime, this mean growth rate is $\sim g c_s / c_{\text{half},s}$, where c_s is the characteristic substrate concentration scale within the front. The latter can be estimated by matching the substrate gradient coming from diffusion outside the colony $\sim c_{\text{f},s} / \{x_{\text{sys}}, r_{\text{sys}}\}$ with the gradient in the growing layer $\sim c_s / l_s$, yielding $c_s \sim l_s c_{\text{f},s} / \{x_{\text{sys}}, r_{\text{sys}}\}$. Thus, $t_c = g^{-1} c_{\text{half},s} \{x_{\text{sys}}, r_{\text{sys}}\} / (l_s c_{\text{f},s})$.

Using these natural scales, we obtain the following dimensionless parameters that govern colony growth:

$$\begin{aligned} \Gamma &\equiv \frac{g c_{\text{f},s} l_s}{k_s \rho \{x_{\text{sys}}, r_{\text{sys}}\}} : \frac{\text{Diffusive/Uptake timescale}}{\text{Growth timescale}}, \\ C &\equiv \frac{c_{\text{f},s}}{c_{\text{half},s}} : \frac{\text{Far-field substrate concentration}}{\text{Half-velocity constant}}, \\ \{\tilde{x}_{\text{sys}}, \tilde{r}_{\text{sys}}\} &= \sqrt{\frac{k_s \rho}{D_s c_{\text{half},s}}} \{x_{\text{sys}}, r_{\text{sys}}\} : \frac{\text{System size}}{\text{Substrate penetration length}}, \\ \{\tilde{X}_{\text{init}}, \tilde{R}_{\text{init}}\} &= \sqrt{\frac{k_s \rho}{D_s c_{\text{half},s}}} \{X_{\text{init}}, R_{\text{init}}\} : \frac{\text{Initial size}}{\text{Substrate penetration length}}. \end{aligned} \quad [2]$$

The first parameter Γ compares the characteristic diffusive timescale l_c^2 / D_s , which is equivalent to the substrate uptake timescale $c_{\text{half},s} / (k \rho)$ since both diffusion and uptake are in quasisteady-state balance within the growing surface layer, with the characteristic timescale t_c for growth. As expected, in the experiments, $\Gamma \ll 1$, which means growth is slow compared to the turnover rate of substrate due to uptake and diffusion in the colony. This implies that c_{in} is always at quasisteady state.

The dimensionless parameter \tilde{x}_{sys} or \tilde{r}_{sys} , which describes a slab-shaped or cylindrical colony, respectively, is the ratio between the overall system size, x_{sys} or r_{sys} , and the substrate penetration length l_s . Since \tilde{x}_{sys} and \tilde{r}_{sys} are large in our experiments, we expect that the qualitative growth behavior does not depend on the precise value of \tilde{x}_{sys} or \tilde{r}_{sys} .

The last dimensionless parameter \tilde{X}_{init} or \tilde{R}_{init} compares the initial width X_{init} or radius R_{init} of a slab-shaped (Fig. 2) or cylindrical (Fig. 1) colony, respectively, with the substrate penetration length l_s . This parameter thus prescribes the initial condition in our theoretical model. In our experiments with cylindrical 3D colonies, $\tilde{R}_{\text{init}} \gg 1$ and $\Gamma \ll 1$ as expected; hence, substrate becomes quickly depleted from the interior of the colony, and growth is localized to the surface boundary layer. We, therefore, expect that the subsequent morphodynamics are independent of the initial colony shape. For this reason, we first consider the slab geometry schematized in Fig. 2*A*, which simplifies the analysis of the morphological instability, and then, extend our analysis to the cylindrical geometry that describes the experiments (Fig. 1*A*).

Continuum Model Recapitulates the Key Experimental Findings. Having established that growth is localized to a thin surface layer, we next ask how this localization influences the subsequent colony morphodynamics. Because only a small fraction of the colony is growing, we expect that the effects of random fluctuations in substrate availability and thus, cellular growth are amplified—potentially engendering this morphological instability. To quantitatively explore this possibility, we first seek a 1D solution of the continuum model equations for the slab geometry (Fig. 2*A*) with a flat surface and then examine its stability to shape perturbations.

To obtain a 1D solution of the flat-slab geometry, we assume that all the variables only depend on the coordinate \tilde{x} along which the front propagates: $\tilde{u}_0 = \tilde{u}_{x,0}(\tilde{x}) \mathbf{e}_x$, $\tilde{p}_0 = \tilde{p}_0(\tilde{x})$, $\tilde{c}_{\text{in},0} = \tilde{c}_{\text{in},0}(\tilde{x})$, and $\tilde{c}_{\text{out},0} = \tilde{c}_{\text{out},0}(\tilde{x})$, where the position of the moving interface $\tilde{X}_0(\tilde{t})$ is only a function of time \tilde{t} , tildes denote dimensionless variables, and the nought subscripts denote the 1D flat-slab solution. As detailed in *SI Appendix*, the solution is given by *SI Appendix*, Eqs. S9 and S10. Fig. 2*B* shows the resulting spatial profile of substrate concentration at different times \tilde{t} for the illustrative case in which the initial colony width $\tilde{X}_{\text{init}} = 10$. The initial leading edge of the colony is shown by the vertical line, and Fig. 2*B*, *Inset* depicts its subsequent position as a function of time. As in the experiments, because $\tilde{X}_{\text{init}} \gg 1$, the substrate is mostly depleted inside the colony, and only the surface boundary layer is able to grow.

Having established the 1D flat-slab solution, we next perform a linear stability analysis of this solution to assess whether this colony is intrinsically unstable to shape perturbations (detailed in *SI Appendix*). In particular, we analyze the rate $\tilde{\omega}(\tilde{k}, \tilde{t})$ at which small periodic perturbations in the colony surface of wave number \tilde{k} , which corresponds to a wavelength $2\pi/\tilde{\lambda}$, grow in time. Thus, if $\tilde{\omega}(\tilde{k}) > 0$, shape perturbations become amplified over time, and the surface of the colony is unstable; however, if $\tilde{\omega}(\tilde{k}) < 0$, the perturbations become suppressed as the colony grows. The results for two exemplary values of \tilde{k} are shown in Fig. 2*C* and *D*. Intriguingly, the shorter-wavelength perturbation with larger $\tilde{k} = 0.8$ is stable, flattening out over time; by contrast, the longer-wavelength perturbation with a smaller $\tilde{k} = 0.328$ is unstable, causing the undulations in the colony surface to amplify as the colony grows.

This wavelength dependence is summarized in Fig. 2*E*, which shows the perturbation growth rate $\tilde{\omega}(\tilde{k})$ evaluated at the initial time for slab-shaped colonies of different initial widths \tilde{X}_{init} ; the simulations of Fig. 2*C* and *D* are indicated by the dots. As mentioned before, we expect that when $\tilde{X}_{\text{init}} \gg 1$, the colony width does not play a role in the stability of the growing front.

In agreement with this expectation, we find that when the colony width substantially exceeds the substrate penetration length, the perturbation growth rate $\tilde{\omega}$ becomes independent of the width, as shown by the collapse of the curves for $\tilde{X}_{\text{init}} \gtrsim 10$. In this limit, the colony is morphologically unstable ($\tilde{\omega} > 0$) at $\tilde{k} < \tilde{k}_c$, where $\tilde{k}_c = 3/4$ is a cutoff wave number—consistent with the results shown in Fig. 2 C and D. Moreover, the perturbation growth rate takes on its maximal value $\tilde{\omega}_{\text{max}}$ at a parameter-free most-unstable wave number \tilde{k}_{max} , which corresponds to a value $\tilde{k}^* \approx 0.328$ in the substrate-depleted limit $\tilde{X}_{\text{init}} \gg 1$. That is, our continuum model predicts that dense colonies of bacteria generically become morphologically unstable as they grow—just as in the experiments. Moreover, this morphological instability is initiated by surface growth of a most-unstable wavelength $\tilde{\lambda}^* \approx 2\pi/0.328$ i.e., we expect $\lambda^* \approx 19.2 \mu\text{m} \sim 20$ to $200 \mu\text{m}$ in the experiments, comparable with the characteristic floret size we observe for *E. coli*.

The linear stability analysis only describes the onset of the morphological instability—but does not incorporate the influence of nonlinearities in the model, which we expect play a crucial role in the roughening over longer times. To explore the ability of our model to capture these additional complexities, we perform full 2D numerical simulations of Eq. 1 over long times ($\tilde{t} \gg 1$) for a growing slab-shaped colony, initially with a flat interface perturbed by random shape fluctuations (SI Appendix). Intriguingly, without injecting additional time-dependent noise, these simulations reproduce key features of the colony roughening revealed by our experiments, as characterized by the power spectral density $S(k, t)$ shown in Fig. 2F; compare these data with the experimental $S(k, t)$ in Fig. 1D. In both cases, $S(k)$ approaches a time-independent form over comparable timescales, eventually exhibiting an apparent power-law decay $\sim k^{-\nu}$ at large k with $\nu \approx 2$ and plateauing at small $k \lesssim k^*$. Thus, taken altogether, these results indicate that despite its simplicity, our active fluid continuum model of growing bacterial colonies captures the essential features of both the morphological instability and the roughening found experimentally.

Continuum Model Reveals How Substrate-Limited Growth Causes Colony Instability. What is the biophysical origin of the morphological instability? Our continuum model provides an answer; for example, compare Fig. 2 C (stable) and D (unstable). In the latter unstable case, the concentration of substrate at the peaks of the perturbed colony surface is larger than in the valleys, resulting in faster subsequent growth at the peaks than in the valleys, which further amplifies the separation between the two. By contrast, in the former stable case, growth at the peaks transverse (in \tilde{z}) to the overall propagation direction \tilde{x} fills in the valleys, which reduces the separation between the two. Thus, differential access to substrate at different locations along the surface of a colony, which in turn, imparts differences in the rate of cellular growth, is the primary mechanism driving colony morphological instability. Indeed, we can quantitatively express this intuition by analyzing the different contributions to the perturbation growth rate described by SI Appendix, Eq. S15 for a given wave number \tilde{k} :

$$\frac{d\tilde{A}}{d\tilde{t}} = \underbrace{\tilde{x}_{\text{sys}} \tilde{c}_0 \tilde{A}}_{\text{Destabilizing}} - \underbrace{\nabla \tilde{p}_1 \cdot \mathbf{e}_x}_{\text{Stabilizing}}, \quad \text{at } \tilde{x} = \tilde{X}_0(\tilde{t}), \quad [3]$$

where $\tilde{A}(\tilde{t})$ is the perturbation amplitude corresponding to the specific \tilde{k} being considered. The first term on the right-hand side corresponds to the driving mechanism of the instability; it

reflects the fact that the concentration of substrate is higher in the peaks than in the valleys of the perturbed front. In particular, the substrate concentration of the 1D solution at the flat surface of an unperturbed colony, $\tilde{c}_0(\tilde{x} = \tilde{X}_0)$, is positive for all values of the wave number \tilde{k} and initial colony width \tilde{X}_{init} —thus, all perturbations are amplified. By contrast, the second term on the right-hand side of Eq. 3 is the leading-order perturbation of the pressure gradient inside the colony and reflects the stabilizing contribution from transverse growth. This stabilizing mechanism becomes very weak for large colonies ($\tilde{X} \gg 1$), where substrate is depleted and growth mainly occurs in the \tilde{x} direction, but it is able to overcome the destabilizing mechanism when $\tilde{k} \gg 1$. This behavior starkly contrasts that of bacterial colonies that are not substrate limited in their interior and thus, grow uniformly at the same rate—for which all wavelengths become stable at sufficiently large colony width $\tilde{X} \gg 1$ (SI Appendix, Fig. S19) since transverse growth is able to smooth out any perturbation.

When They Are Sufficiently Large, Growing Cylindrical Colonies Exhibit the Same Morphological Instability. In our experiments, the shapes of the 3D bacterial colonies do not correspond to a slab geometry, as their initial shapes are cylindrical (Fig. 1). However, the same biophysical ideas apply. We, therefore, employ the same theoretical framework and perform the equivalent linear stability analysis and time-dependent numerical simulations but for the cylindrical case (as detailed in SI Appendix, Figs. S20–S22). In this case, however, the shape perturbations to the colony surface can be either in the direction along the cylinder axis or along its azimuth—denoted by z or θ in Fig. 1B. Thus, we describe the harmonic perturbations using both the axial wave number \tilde{k} and azimuthal mode number m .

The results of the linear stability analysis are summarized in Fig. 3 A and B. The color plots show the perturbation growth rate $\tilde{\omega}$ as a function of \tilde{k} and the ratio between the initial colony radius and the substrate penetration length, \tilde{R}_{init} , for two different azimuthal modes. Redder regions indicate increasingly unstable perturbations (larger $\tilde{\omega} > 0$), while blacker regions indicate increasingly stable perturbations (more negative $\tilde{\omega} < 0$). The orange dashed curve corresponds to the loci of the most-unstable mode ($\tilde{k}_{\text{max}}, \tilde{\omega}_{\text{max}}$) for each corresponding value of m .

First, we examine the case of axisymmetric perturbations ($m = 0$). As shown at the top of Fig. 3A, large colonies ($\tilde{R}_{\text{init}} \gg 1$) are unstable to perturbations at $\tilde{k} < \tilde{k}_c = 3/4$, with a most-unstable wave number $\tilde{k}^* = 0.328$ —just as in the slab geometry, as expected. This most-unstable mode is shown in the 3D rendering in Fig. 3 A, Right. As shown at the bottom of Fig. 3A, with decreasing $\tilde{R}_{\text{init}} \lesssim 1$, fluctuations in the growing surface layer increasingly dominate the morphodynamics, and axial wave numbers $\tilde{k} \lesssim 1/\tilde{R}_{\text{init}}$ are increasingly unstable, as expected. Intriguingly, however, small- \tilde{k} modes become stabilized for intermediate colony sizes ($10^0 \lesssim \tilde{R}_{\text{init}} \lesssim 10^1$)—which likely reflects a nontrivial interplay between substrate availability and colony growth in these geometries.

Next, we study the case of nonaxisymmetric perturbations, taking $m = 8$ as an example. As shown at the bottom of Fig. 3B, in this case, all axial wave numbers are instead stable at small $\tilde{R}_{\text{init}} \lesssim 1$ —indicating that the stabilizing influence of transverse growth overcomes the morphological instability. However, as expected, large colonies ($\tilde{R}_{\text{init}} \gg 1$) are again unstable to small- \tilde{k} perturbations but stable to large- \tilde{k} perturbations, with a most-unstable wave number $\tilde{k}^* = 0.328$ —just as in the slab

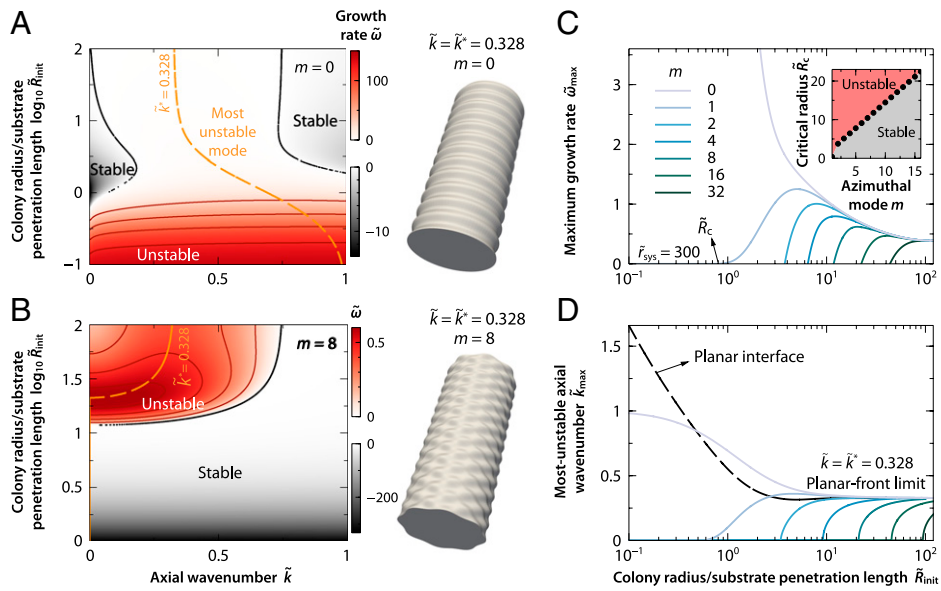


Fig. 3. A continuum model of a growing cylindrical colony reveals a similar morphological instability. (*A*, Left and *B*, Left) Color plots of the small-time growth rate $\tilde{\omega}$ of perturbations as a function of the axial wave number \tilde{k} and the dimensionless ratio \tilde{R}_{init} between the initial colony radius and the substrate penetration length for dimensionless system radius $\tilde{r}_{\text{sys}} = 300$. The azimuthal mode is $m = 0$ (axisymmetric perturbation) in *A* and $m = 8$ (nonaxisymmetric perturbation) in *B*. The orange dashed curves indicate the loci of the most-unstable mode, indexed by $(\tilde{\omega}_{\text{max}}, \tilde{k}_{\text{max}})$. When $\tilde{R}_{\text{init}} \gg 1$, $\tilde{k}_{\text{max}}(m) \rightarrow \tilde{k}^* = 0.328$ as found for a planar slab geometry. (*A*, Right and *B*, Right) 3D renderings of a colony at the indicated values of m and $\tilde{k} = \tilde{k}^* = 0.328$, which corresponds to the most-unstable mode for a planar slab. (*C*) Maximum growth rate of perturbations $\tilde{\omega}_{\text{max}} = \tilde{\omega}(\tilde{k}_{\text{max}}, m)$ as a function of \tilde{R}_{init} for different azimuthal modes m . (*C*, Inset) Critical radius \tilde{R}_c beyond which each nonaxisymmetric mode becomes unstable. For $\tilde{R} < \tilde{R}_c$, all modes are initially stable (i.e., decaying with growth). (*D*) The most-unstable wave number $\tilde{k}_{\text{max}}(m)$ as a function of \tilde{R}_{init} for the same values of m shown in *C*.

geometry and the $m = 0$ case. This most-unstable mode is shown in the 3D rendering in Fig. 3 *B, Right*. Thus, when colonies become large enough for growth to be localized to their surface, the morphological instability becomes independent of colony size or geometry.

To further compare the influence of axisymmetric ($m = 0$) and nonaxisymmetric ($m \neq 0$) perturbations, we examine the variation of the growth rate $\tilde{\omega}_{\text{max}}$ with \tilde{R}_{init} for the most-unstable mode, indicated by the orange dashed curves in Fig. 3 *A* and *B*. The results are shown in Fig. 3 *C* for different azimuthal mode numbers m ; the corresponding most-unstable axial wave number \tilde{k}_{max} is shown in Fig. 3 *D*. As expected, we find that the results for both axisymmetric and nonaxisymmetric perturbations converge to the same curve when $\tilde{R}_{\text{init}} \gg 1$ (the collapse of the curves on the right in Fig. 3 *C* and *D*), which corresponds to the size-independent curve obtained for a slab-shaped colony shown in Fig. 2*E*. This collapse again corroborates the finding that, when colonies become large enough for growth to be localized to their surface, the morphological instability appears to become independent of colony size or geometry. Moreover, for each nonaxisymmetric mode, there is a critical dimensionless colony radius, $\tilde{R}_c(\tilde{k}, m)$, below which the growing colony is stable for all axial wave numbers \tilde{k} (i.e., $\tilde{\omega} < 0$) as shown in Fig. 3 *C*, *Inset*—again indicating that the stabilizing influence of transverse growth overcomes the morphological instability for these modes. Indeed, the data in Fig. 3 *C*, *Inset* indicate that this critical radius varies as $\tilde{R}_c = 3m/4$, which agrees with the cutoff wave number obtained for a planar front, $\tilde{k}_c = 3/4$. Hence, modes with a larger value of m need larger values of \tilde{R}_{init} to merge into the planar slab limit. That is, more nonaxisymmetric modes become unstable when the radius of the colony increases; these grow with the same rate and a parameter-free most-unstable wavelength corresponding to the slab geometry i.e., $\tilde{\lambda}_{\text{max}}(\tilde{R}_{\text{init}} \gg 1) \rightarrow$

$\tilde{\lambda}^* \simeq 19.2$ or equivalently, $\tilde{k}^* = 0.328$. We confirm this behavior in which more nonaxisymmetric modes become unstable via full numerical simulations (SI Appendix, Figs. S21 and S22). Further investigating these interesting morphodynamic features that arise due to the interplay between substrate availability and cellular growth, mediated by the geometry of the colony surface, will be a useful extension of our theoretical framework.

Taken together, our theoretical and simulation results for cylindrical colonies imply that when growth is localized to the surface of a colony—as is inherently the case when the colony becomes sufficiently large and dense—generic morphological instability and roughening arise, independent of the initial colony size or geometry and without requiring a specific nutrient environment or cell type, just as in our experiments. The instability is characterized by a most-unstable wavelength whose theoretically predicted size agrees well with our experimental observations. Our numerical simulations show that the roughening, in turn, arises from the nonlinear long-time growth of small-scale perturbations over many scales, with a characteristic power spectrum whose key features also agree well with our experimental observations.

Discussion

Despite the ubiquity of bacteria in natural 3D environments, the morphodynamics of colonies growing in 3D has remained largely unexplored. One reason is the challenge of visualizing bacteria in opaque 3D media (e.g., soil or tissues and organs). We overcame this challenge by performing experiments in transparent granular hydrogel matrices. Strikingly, we found that large, dense colonies growing in 3D undergo a generic morphological instability as well as roughening, adopting the same characteristic broccoli-like morphology independent of variations in cell type and environmental conditions. We elucidated the instability using a continuum active fluid model that incorporates the diffusion and uptake of a

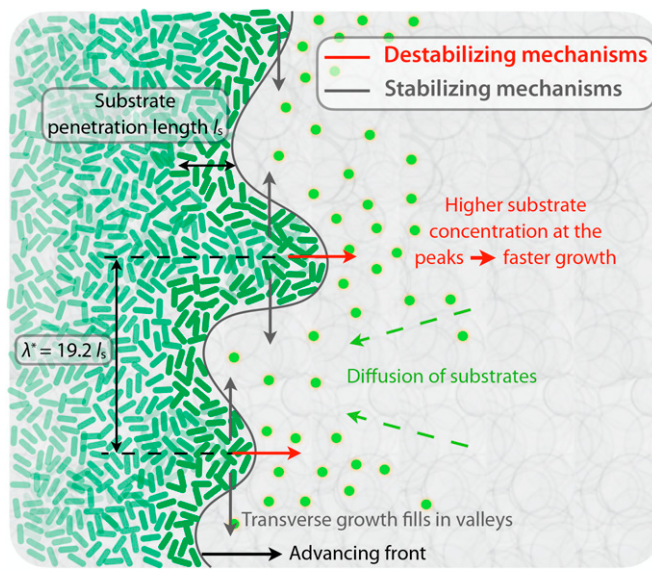


Fig. 4. Biophysical mechanisms by which a growing colony is stabilized (gray) or destabilized (red). Substrates diffuse from the surroundings and are consumed by the cells in the colony (green), resulting in subsequent growth and outward colony expansion. The competition between substrate diffusion and consumption results in a small penetration length, causing growth to be localized at the surface of the colony. Growth transverse to the overall outward expansion direction fills in valleys and is thus stabilizing, while the increased availability of nutrients at peaks enables them to grow faster and is thus destabilizing. The competition between these mechanisms establishes the most-unstable wavelength λ^* that emerges from our continuum model.

substrate essential for growth coupled to cellular proliferation. In particular, we found that the sine qua non condition for the instability is substrate depletion in the interior of the colony, causing the colony to expand via growth only at its surface. As schematized in Fig. 4, this surface growth amplifies perturbations in the overall colony shape—which inevitably arise in complex settings. In particular, we find that, in addition to roughening over a broad range of small spatial scales, there exists a universal most-unstable wavelength $\lambda^* \simeq 19.2 l_s$, where l_s is the substrate penetration length into the colony. Hence, our experimental and modeling results reflect a key difference between growing in 2D and 3D in terms of access to critical substrates; while 2D colonies may access the substrates needed for growth from the third dimension and only become morphologically unstable when growth is limited to a peripheral layer (28, 31, 32, 55, 91–93, 103–105), large 3D colonies inevitably become internally substrate limited even under globally nutrient-replete conditions, eventually guaranteeing rough growth at their surface.

Roughening of 3D Growing Colonies. Surface growth is known to cause roughening in diverse processes ranging from the growth of snowflakes and agglomeration of colloids to the formation of conductive dendrites that impede the operation of batteries (89, 90, 103, 106–117). Similar roughening also arises in the growth of mammalian cell clusters in nutrient-depleted spaces (79, 100, 118). Despite the strikingly different physical details, many of these processes exhibit remarkably universal growth dynamics and morphologies that can be described using the Edwards–Wilkinson (EW) or Kardar–Parisi–Zhang (KPZ) continuum growth models (or variations) (89, 90, 103, 106–117). Hence, to explore if growing 3D bacterial colonies share some of these universal characteristics, we computed the power spectrum $S(k, t)$ and the local roughness $w_{loc}(L, t)$ of the colony surface profiles. As our data showing apparent power-law scaling only span at most one decade of k between the limits k_c and $2\pi/l_s$, we do not make strong claims regarding scaling in our system; nevertheless,

we found similar results across the multiple cell types and environmental conditions tested, suggesting that our results reflect generic features of growing 3D bacterial colonies. As expected, the majority of the power corresponds to length scales around the most-unstable wavelength λ^* ; as in many other growing systems, the spectra also appear to exhibit a power-law decay, $S(k, t) \sim k^{-\nu}$, with $\nu \approx 2.3$ at large k —reflecting the multiscale nature of the surface roughening. Moreover, as in many other growing systems, the local roughness appears to scale with the length L of the analyzed region as $w_{loc} \sim L^\alpha$ —in our case, with $\alpha \approx 0.7$. The measured power spectra decay and roughness exponents agree with the prediction of so-called Family–Vicsek dynamic scaling in 1D, $\nu = 1 + 2\alpha$, which suggests that the surface of growing colonies is self-similar (89). Thus, analogous to many other growing systems, 3D bacterial colonies appear to adopt universal, self-similar, fractal shapes as they grow, independent of their starting geometry. Furthermore, the fact that the relation between the local roughness exponent and the power spectrum corresponds to 1D Family–Vicsek scaling supports the idea that the geometry or dimension of the front is not relevant for determining the stability or characteristics of the roughening process, when growth is localized to the surface.

Intriguingly, the measured local roughness exponent $\alpha \approx 0.7$ appears to be different from the value $\alpha = 1/2$ characteristic of the EW and KPZ universality classes. Nonetheless, these data suggest that growing 3D colonies become rougher than many other growing systems that are well described by the KPZ model. Values of α larger than $1/2$ have been found in other systems, typically when quenched disorder is present (89)—for instance, in fluid flows through porous media (109–112, 117, 119), burning fronts (113), directed percolation (114, 120–122), or bacterial colonies growing on 2D gels (91, 103–105). What mechanisms could explain the large roughness exponent in our experiments? One possibility is that it reflects unstable growth associated with the coupling between cellular growth and substrate diffusion/uptake, as predicted by linear stability analysis of our model and as described for other reaction–diffusion systems employed to model 2D growing colonies (91, 105). The fact that the experimental power spectra exhibit a range of wavelengths where the power takes maximum values may be indicative of unstable growth during the expansion of the 3D colony. However, another possibility is that the large value of α reflects the influence of the granular disorder of the hydrogel matrices. We neglected this complexity in our model for simplicity; however, we note that disorder is indeed thought to give rise to anomalously large growth exponents (89, 91, 103–105, 109–113, 117, 120–126). Building on our work to study the influence of this added complexity will be an important direction for the future.

Strengths and Limitations of Our Theoretical Model. Given the complexities inherent in the experiments and the simplicity of our active fluid model, can we still make quantitative comparisons between experiments and theory? As summarized below, our theoretical analysis captures the four essential features of the experimental observations: (1) the width of the actively growing layer of cells at each colony surface, (2) the time at which colonies begin to become unstable and roughen, (3) the characteristic wavelength that bounds colony shape fluctuations at large scales, and (4) the scaling behavior of the smaller-scale fluctuations in the rough morphology that colonies eventually produce.

We expect that feature (1) is set by the penetration length of the growth-limiting essential substrate, which we estimated using our theory as $l_s = \sqrt{D_s c_{half,s}/(k_s \rho)} \sim 1$ to $9 \mu\text{m}$ (*SI Appendix*, Table S1). Our experiments yielded a comparable value; in all

the experiments, independent of other cell properties, substrate availability, or initial geometry, we directly visualized a thin layer of fluorescent bacteria (which indicates cells are metabolically active) extending over a distance $\lesssim 20 \mu\text{m}$ from the colony front. Consistent with our findings, previous theoretical work on 2D colonies has also indicated that a rough front arises when growth occurs only in a sufficiently thin layer located close to the advancing front (i.e., under globally scarce nutrient conditions in the case of a 2D colony) (28, 31, 32, 55, 91–93).

The timescale for the colony to expand by the width of the surface layer, which we expect sets feature (2), is predicted by our theory to be $t_c \sim 6$ to 50 h (*SI Appendix*, Table S1). Consistent with this expectation, in all the experiments, we found that colonies become rough after several hours—which also agrees well with our full numerical simulations in the substrate-depleted limit (Fig. 2F and *SI Appendix*, Figs. S21 and S22).

Regarding features (3) and (4), our experiments reveal that the power spectrum of shape fluctuations $S(k, t)$ plateaus for $k \ll 2\pi/\lambda_c$ and exhibits a power-law decay for $k \gtrsim 2\pi/\lambda_c$, where the characteristic cross-over wavelength is $\lambda_c \approx 60$ to 600 μm for *E. coli*. As shown in *SI Appendix*, Fig. S23A, analysis of a linearized form of our model similarly implies a plateau in the power spectrum for small k , for which the growth rate $\omega \rightarrow 0$ (with noise injecting additional power), and a power-law decay for large k —with the characteristic wavelength demarcating the transition between these regimes predicted to be $\lambda_c = (8\pi/3)l_s \sim 10$ to 70 μm , roughly comparable with the experimental values. However, the power-law exponent predicted by the linear analysis, $\nu = 1$ (*SI Appendix*, Fig. S23A), differs from that found in the experiments, $\nu \approx 2.3$, indicating that nonlinear effects are crucial. Along the same lines, the linear regime of our model, in which some wavelength perturbations decay and others grow without bound, cannot directly account for the saturation of the power spectra observed in the experiments at long time, where $S(k, t)$ reaches a fixed curve—again suggesting a pivotal role of nonlinearities in the system. Indeed, our long-time 2D simulations of the full model better reproduce key features of the experiments: the development of the experimental scaling, the plateau around the low- k most-unstable mode, and the saturation of the amplitude of the unstable modes and lack of subsequent coarsening over timescales similar to those of the experiments, as shown in Fig. 2F. This agreement between experiment and theory is noteworthy given the simplicity of the model. Moreover, the experiments revealed a similar morphological instability and roughening in four different species of bacteria having different natural habits and physiologies, highlighting the generality of this phenomenon as predicted by the theory. Finally, we note that recent *in vivo* studies have reported similar rough morphologies of bacterial aggregates growing in diverse 3D environments, such as snow (127), microgels prevalent in marine environments (128, 129), mouse urine (130), and sludge (131, 132). Further work elucidating the nonlinear physics underlying roughening—for example, using direct numerical simulations of the noisy version of Eq. 1 with either thermal or quenched noise or via expanding an interface equation to obtain the leading nonlinearities (at least in the limit of a thin growing surface layer), possibly along with renormalization group analysis (89)—will, therefore, be important.

Nevertheless, our model has limitations and does not quantitatively reproduce the entirety of the experimental findings—suggesting refinements for future work. For example, we note that while our quantitative analysis focused on experiments with *E. coli*—given that the physical parameters describing these cells (*SI Appendix*, Table S1) are well characterized, that the cellular fluorescence enabled high-resolution

imaging via confocal microscopy, and that this strain does not appreciably secrete extracellular materials—we also observed a similar morphological instability for the biofilm formers *V. cholerae*, *P. aeruginosa*, and *K. sucofermentans*. However, we note that the characteristic floret wavelength for these latter three species is noticeably larger than for *E. coli* (*SI Appendix*, Figs. S10–S14 and S24). This difference could reflect the greater uncertainty in the substrate penetration length l_s for these species, which may in reality be larger than our estimated value. It may also reflect the added influence of the extracellular polymeric matrix secreted by the cells as they grow, which potentially leads to additional complexities. Other experimental effects that are also not contained within the model—but may nevertheless play a role—include the granularity and deformability of the hydrogel matrices noted earlier, the mechanical properties of and cellular orientations within the bacterial colony, variations of cellular density within the growing layer, and limitations on the space and amount of nutrient available to the growing colony. Finally, we note that while the cylindrical geometry of the initial inoculum employed in the experiments incorporates curvature that is a feature of many growing natural colonies, additional complexities may arise from the coupling between growth in the azimuthal and axial directions beyond the features described in Fig. 3.

Implications for Microbiology. Our work demonstrates that, large, dense, 3D bacterial colonies cannot avoid developing unstable and rough surfaces as they grow. What are the biological implications of these morphodynamics? The highly branched colony shapes studied here are characterized by large surface area-to-volume ratios, which likely promote the exposure of metabolically active cells at the colony surfaces to their surroundings. Thus, we speculate that the morphological instability and roughening of growing bacterial colonies could be harmful to them by increasing susceptibility to antibiotics (61–63) or phages (64) but could also be beneficial by providing more space for mutants to grow, thereby supporting genetic diversity (56, 58, 59, 67–72) and potentially enabling colonies to be more resilient against environmental changes (65, 66).

Cell–cell signaling might also be affected by these morphodynamics since different regions of the branched surface of a colony could become decoupled from each other—which in turn, could also affect overall colony function and internal colony morphology (133). Previous work on 2D growing colonies has shown metabolic cooperation between cells growing at the periphery of the colony and those located in the interior—ion channels enable long-range electric signaling between both regions of the colony, giving rise to spatially propagating metabolic waves (134–139). Hence, although our results suggest that the core of 3D colonies plays a passive role in the colony morphodynamics, the interaction and signaling between the growing surface layer and the core may have important consequences for the global function and structure of the colony.

More broadly, given our finding of morphological instability and roughening that emerge generically from the coupling between diffusion and uptake of essential substrates for cellular growth in 3D, we expect that similar behavior could arise in other growing systems, with implications for the evolution of form and function (50, 58, 140–142). Indeed, similar 3D patterns of rough growth have been observed in other living systems, namely in multicellular clusters of *Saccharomyces cerevisiae*, usually referred to as “snowflake yeast,” or in aggregation clusters of the green alga *Volvox carteri*. Recent research has shown that the sizes and morphologies of these clusters are crucially determined by growth and crowding-induced mechanical stresses coupled to environment conditions (143–147). These works have suggested

the tantalizing idea that the morphological adaptation of large 3D clusters to environmental constraints could provide insight into the origins of multicellularity. Altogether, our experimental approach and findings, as well as our theoretical framework, could provide a foundation for these promising future avenues for research.

Materials and Methods

Imaging Growth of Bacterial Colonies. For the experiments with fluorescent *E. coli*, we used a Nikon A1R+ inverted laser-scanning confocal microscope maintained at $30^{\circ}\text{C} \pm 1^{\circ}\text{C}$ to acquire vertical stacks of planar fluorescence images separated by $2.58\ \mu\text{m}$ in depth. For the experiments with *V. cholerae*, *P. aeruginosa*, and *K. sucofermentans*, we used a Sony α 6300 camera with a Thorlabs 6.5 \times Zoom Lens to acquire color images. Between imaging time points, the samples were placed in a 37°C incubator (for *V. cholerae*) or a 30°C (for *P. aeruginosa* and *K. sucofermentans*). As time progressed, the colonies continued to grow until at long times ($\gtrsim 100$ h), when colony expansion ceased presumably due to complete substrate depletion.

Data, Materials, and Software Availability. The data and codes that support the plots and findings of this study are available on Zenodo (148). All other data are included in the article and/or supporting information.

ACKNOWLEDGMENTS. A.M.-C. acknowledges support from the Princeton Center for Theoretical Science and Human Frontier Science Program Grant

LT000035/2021-C. R.K.B. acknowledges support from the Presidential Postdoctoral Research Fellows Program. H.N.L. acknowledges support from the Lidow Independent Work/Senior Thesis Fund at Princeton University. This material is also based upon work supported by NSF Graduate Research Fellowship Program Grant DGE-2039656 (to A.M.H.). N.S.W. acknowledges support from NSF Center for the Physics of Biological Function Grant PHY-1734030 and NIH Grant R01 GM082938. S.S.D. acknowledges support from NSF Grants CBET-1941716, DMR-2011750, and EF-2124863 as well as the Eric and Wendy Schmidt Transformative Technology Fund, the New Jersey Health Foundation, the Pew Biomedical Scholars Program, and the Princeton OA Fund. We thank Daniel Amchin, Alejandro Sevilla, Howard Stone, and Sankaran Sundaresan for thoughtful discussions and Sebastian Gonzalez La Corte for assistance with experiments using *P. aeruginosa*. We also thank the laboratories of Bob Austin, Bonnie Bassler, and Zemer Gitai for providing strains of *E. coli*, *V. cholerae*, and *P. aeruginosa*, respectively.

Author affiliations: ^aPrinceton Center for Theoretical Science, Princeton University, Princeton, NJ 08544; ^bDepartment of Chemical and Biological Engineering, Princeton University, Princeton, NJ 08544; ^cThe Andlinger Center for Energy and the Environment, Princeton University, Princeton, NJ 08544; ^dLewis-Sigler Institute for Integrative Genomics, Princeton University, Princeton, NJ 08544; and ^eDepartment of Molecular Biology, Princeton University, Princeton, NJ 08544

Author contributions: A.M.-C., T.B., N.S.W., and S.S.D. designed research; A.M.-C., T.B., R.K.B., H.N.L., A.M.H., and S.S.D. performed research; A.M.-C., T.B., N.S.W., and S.S.D. contributed new reagents/analytic tools; A.M.-C., T.B., R.K.B., H.N.L., A.M.H., N.S.W., and S.S.D. analyzed data; and A.M.-C., N.S.W., and S.S.D. wrote the paper.

1. P. Stoodley, K. Sauer, D. G. Davies, J. W. Costerton, Biofilms as complex differentiated communities. *Annu. Rev. Microbiol.* **56**, 187–209 (2002).
2. A. Persat *et al.*, The mechanical world of bacteria. *Cell* **161**, 988–997 (2015).
3. H. C. Flemming *et al.*, Biofilms: An emergent form of bacterial life. *Nat. Rev. Microbiol.* **14**, 563–575 (2016).
4. A. Martínez-Calvo, C. Trenado-Yuste, S. S. Datta, Active transport in complex environments. arXiv [Preprint] (2021). <https://arxiv.org/abs/2108.07011> (Accessed 19 August 2021).
5. P. E. Kolenbrander, Oral microbial communities: Biofilms, interactions, and genetic systems. *Annu. Rev. Microbiol.* **54**, 413–437 (2000).
6. K. Werdan *et al.*, Mechanisms of infective endocarditis: Pathogen-host interaction and risk states. *Nat. Rev. Cardiol.* **11**, 35–50 (2014).
7. C. M. Dejea *et al.*, Patients with familial adenomatous polyposis harbor colonic biofilms containing tumorigenic bacteria. *Science* **359**, 592–597 (2018).
8. P. D. Schloss, J. Handelsman, Toward a census of bacteria in soil. *PLoS Comput. Biol.* **2**, e92 (2006).
9. R. Hayat, S. Ali, U. Amara, R. Khalid, I. Ahmed, Soil beneficial bacteria and their role in plant growth promotion: A review. *Ann. Microbiol.* **60**, 579–598 (2010).
10. K. Drescher, Y. Shen, B. L. Bassler, H. A. Stone, Biofilm streamers cause catastrophic disruption of flow with consequences for environmental and medical systems. *Proc. Natl. Acad. Sci. U.S.A.* **110**, 4345–4350 (2013).
11. R. Rusconi, M. Garren, R. Stocker, Microfluidics expanding the frontiers of microbial ecology. *Annu. Rev. Biophys.* **43**, 65–91 (2014).
12. T. Liu, Y. F. Cheng, M. Sharma, G. Voordouw, Effect of fluid flow on biofilm formation and microbiologically influenced corrosion of pipelines in oilfield produced water. *J. Petrol. Sci. Eng.* **156**, 451–459 (2017).
13. H. Fujikawa, M. Matsushita, Fractal growth of *Bacillus subtilis* on agar plates. *J. Phys. Soc. Jpn.* **58**, 3875–3878 (1989).
14. E. Ben-Jacob *et al.*, Generic modelling of cooperative growth patterns in bacterial colonies. *Nature* **368**, 46–49 (1994).
15. J. A. Shapiro, The significances of bacterial colony patterns. *BioEssays* **17**, 597–607 (1995).
16. D. A. Kessler, H. Levine, Fluctuation-induced diffusive instabilities. *Nature* **394**, 556–558 (1998).
17. M. Matsushita *et al.*, Interface growth and pattern formation in bacterial colonies. *Physica A* **249**, 517–524 (1998).
18. E. Ben-Jacob, I. Cohen, H. Levine, Cooperative self-organization of microorganisms. *Adv. Phys.* **49**, 395–554 (2000).
19. A. Seminara *et al.*, Osmotic spreading of *Bacillus subtilis* biofilms driven by an extracellular matrix. *Proc. Natl. Acad. Sci. U.S.A.* **109**, 1116–1121 (2012).
20. C. Fei *et al.*, Nonuniform growth and surface friction determine bacterial biofilm morphology on soft substrates. *Proc. Natl. Acad. Sci. U.S.A.* **117**, 7622–7632 (2020).
21. L. Xiong *et al.*, Flower-like patterns in multi-species bacterial colonies. *eLife* **9**, e48885 (2020).
22. J. Müller, W. Van Saarloos, Morphological instability and dynamics of fronts in bacterial growth models with nonlinear diffusion. *Phys. Rev. E Stat. Nonlin. Soft Matter Phys.* **65**, 061111 (2002).
23. R. Tokita *et al.*, Pattern formation of bacterial colonies by *Escherichia coli*. *J. Phys. Soc. Jpn.* **78**, 074005 (2009).
24. F. Beroz *et al.*, Verticalization of bacterial biofilms. *Nat. Phys.* **14**, 954–960 (2018).
25. J. Yan *et al.*, Mechanical instability and interfacial energy drive biofilm morphogenesis. *eLife* **8**, e43920 (2019).
26. N. Luo, S. Wang, J. Lu, X. Ouyang, L. You, Collective colony growth is optimized by branching pattern formation in *Pseudomonas aeruginosa*. *Mol. Syst. Biol.* **17**, e10089 (2021).
27. E. Ben-Jacob, D. S. Coffey, H. Levine, Bacterial survival strategies suggest rethinking cancer cooperativity. *Trends Microbiol.* **20**, 403–410 (2012).
28. F. D. Farrell, O. Hallatschek, D. Maranduzzo, B. Waclaw, Mechanically driven growth of quasi-two-dimensional microbial colonies. *Phys. Rev. Lett.* **111**, 168101 (2013).
29. X. Wang, H. A. Stone, R. Golestanian, Shape of the growing front of biofilms. *New J. Phys.* **19**, 125007 (2017).
30. A. Tam *et al.*, Nutrient-limited growth with non-linear cell diffusion as a mechanism for floral pattern formation in yeast biofilms. *J. Theor. Biol.* **448**, 122–141 (2018).
31. R. J. Allen, B. Waclaw, Bacterial growth: A statistical physicist's guide. *Rep. Prog. Phys.* **82**, 016601 (2019).
32. M. R. Mattei *et al.*, Continuum and discrete approach in modeling biofilm development and structure: A review. *J. Math. Biol.* **76**, 945–1003 (2018).
33. T. Bhattacharjee, D. B. Amchin, J. A. Ott, F. Kratz, S. S. Datta, Chemotactic migration of bacteria in porous media. *Biophys. J.* **120**, 3483–3497 (2021).
34. T. Bhattacharjee, D. B. Amchin, R. Alert, J. A. Ott, S. S. Datta, Chemotactic smoothing of collective migration. *eLife* **11**, e71226 (2022).
35. R. Alert, A. Martínez-Calvo, S. S. Datta, Cellular sensing governs the stability of chemotactic fronts. *Phys. Rev. Lett.* **128**, 148101 (2022).
36. A. Golden, I. Dukovski, D. Segre, K. S. Korolev, Growth instabilities shape morphology and genetic diversity of microbial colonies. *Phys. Biol.* **19**, 056005 (2022).
37. I. Klapper, J. Dockery, Finger formation in biofilm layers. *SIAM J. Appl. Math.* **62**, 853–869 (2002).
38. D. Volson, S. Cookson, J. Hasty, L. S. Tsimring, Biomechanical ordering of dense cell populations. *Proc. Natl. Acad. Sci. U.S.A.* **105**, 15346–15351 (2008).
39. I. Klapper, J. Dockery, Mathematical description of microbial biofilms. *SIAM Rev.* **52**, 221–265 (2010).
40. D. R. Espeso, A. Carpio, B. Einarsson, Differential growth of wrinkled biofilms. *Phys. Rev. E Stat. Nonlin. Soft Matter Phys.* **91**, 022710 (2015).
41. C. Givero, M. Verani, P. Ciarletta, Branching instability in expanding bacterial colonies. *J. R. Soc. Interface* **12**, 20141290 (2015).
42. C. Givero, P. Ciarletta, On the morphological stability of multicellular tumour spheroids growing in porous media. *Eur. Phys. J. E Soft Matter* **39**, 92 (2016).
43. D. Dell'Arciprete *et al.*, A growing bacterial colony in two dimensions as an active nematic. *Nat. Commun.* **9**, 4190 (2018).
44. S. Srinivasan, C. N. Kaplan, L. Mahadevan, A multiphase theory for spreading microbial swarms and films. *eLife* **8**, e42697 (2019).
45. P. Pearce *et al.*, Flow-induced symmetry breaking in growing bacterial biofilms. *Phys. Rev. Lett.* **123**, 258101 (2019).
46. R. Hartmann *et al.*, Emergence of three-dimensional order and structure in growing biofilms. *Nat. Phys.* **15**, 251–256 (2019).
47. M. R. Shaebani, A. Wysocki, R. G. Winkler, G. Gompper, H. Rieger, Computational models for active matter. *Nat. Rev. Phys.* **2**, 181–199 (2020).
48. Y. Yang, H. Levine, Leader-cell-driven epithelial sheet fingering. *Phys. Biol.* **17**, 046003 (2020).
49. S. C. Takatori, K. K. Mandadapu, Motility-induced buckling and glassy dynamics regulate three-dimensional transitions of bacterial monolayers. arXiv [Preprint] (2020). <https://arxiv.org/abs/2003.05618> (Accessed 12 March 2020).
50. Y. G. Pollack, P. Bittihn, R. Golestanian, A competitive advantage through fast dead matter elimination in confined cellular aggregates. *New J. Phys.* **24**, 073003 (2022).
51. J. Nijjer *et al.*, Mechanical forces drive a reorientation cascade leading to biofilm self-patterning. *Nat. Commun.* **12**, 6632 (2021).
52. M. Basaran, Y. I. Yaman, T. C. Yüce, R. Vetter, A. Kocabas, Large-scale orientational order in bacterial colonies during inward growth. *eLife* **11**, e72187 (2022).
53. A. Xia, H. Chen, Y. Huang, X. Zhu, Q. Liao, Mathematical modeling of intercellular interactions within the biofilm. *Trends Microbiol.* **30**, 925–929 (2022).
54. D. Rodriguez, B. Einarsson, A. Carpio, Biofilm growth on rugose surfaces. *Phys. Rev. E Stat. Nonlin. Soft Matter Phys.* **86**, 061914 (2012).
55. G. Melaugh *et al.*, Shaping the growth behaviour of biofilms initiated from bacterial aggregates. *PLoS One* **11**, e0149683 (2016).

56. F. D. Farrell, M. Gralka, O. Hallatschek, B. Waclaw, Mechanical interactions in bacterial colonies and the surfing probability of beneficial mutations. *J. R. Soc. Interface* **14**, 20170073 (2017).
57. M. R. Warren *et al.*, Spatiotemporal establishment of dense bacterial colonies growing on hard agar. *eLife* **8**, e41093 (2019).
58. M. J. I. Müller, B. I. Neugeboren, D. R. Nelson, A. W. Murray, Genetic drift opposes mutualism during spatial population expansion. *Proc. Natl. Acad. Sci. U.S.A.* **111**, 1037–1042 (2014).
59. C. D. Nadell, K. Drescher, K. R. Foster, Spatial structure, cooperation and competition in biofilms. *Nat. Rev. Microbiol.* **14**, 589–600 (2016).
60. W. Liu, T. A. Tokuyasu, X. Fu, C. Liu, The spatial organization of microbial communities during range expansion. *Curr. Opin. Microbiol.* **63**, 109–116 (2021).
61. M. Whiteley *et al.*, Gene expression in *Pseudomonas aeruginosa* biofilms. *Nature* **413**, 860–864 (2001).
62. T. F. Mah *et al.*, A genetic basis for *Pseudomonas aeruginosa* biofilm antibiotic resistance. *Nature* **426**, 306–310 (2003).
63. D. Nguyen *et al.*, Active starvation responses mediate antibiotic tolerance in biofilms and nutrient-limited bacteria. *Science* **334**, 982–986 (2011).
64. W. O. H. Hughes, J. J. Boomsma, Genetic diversity and disease resistance in leaf-cutting ant societies. *Evolution* **58**, 1251–1260 (2004).
65. A. R. Hughes, B. D. Inouye, M. T. Johnson, N. Vellend, Ecological consequences of genetic diversity. *Ecol. Lett.* **11**, 609–623 (2008).
66. T. B. H. Reusch, A. Ehlers, A. Hämerli, B. Worm, Ecosystem recovery after climatic extremes enhanced by genotypic diversity. *Proc. Natl. Acad. Sci. U.S.A.* **102**, 2826–2831 (2005).
67. O. Hallatschek, P. Hersen, S. Ramanathan, D. R. Nelson, Genetic drift at expanding frontiers promotes gene segregation. *Proc. Natl. Acad. Sci. U.S.A.* **104**, 19926–19930 (2007).
68. O. Hallatschek, D. R. Nelson, Gene surfing in expanding populations. *Theor. Popul. Biol.* **73**, 158–170 (2008).
69. O. Hallatschek, D. R. Nelson, Life at the front of an expanding population. *Evolution* **64**, 193–206 (2010).
70. K. S. Korolev, M. Avlund, O. Hallatschek, D. R. Nelson, Genetic demixing and evolution in linear stepping stone models. *Rev. Mod. Phys.* **82**, 1691–1718 (2010).
71. J. Kayser, C. F. Schreck, M. Gralka, D. Fusco, O. Hallatschek, Collective motion conceals fitness differences in crowded cellular populations. *Nat. Ecol. Evol.* **3**, 125–134 (2018).
72. S. Chu, M. Kardar, D. R. Nelson, D. A. Beller, Evolution in range expansions with competition at rough boundaries. *J. Theor. Biol.* **478**, 153–160 (2019).
73. G. T. Fortune, N. M. Oliveira, R. E. Goldstein, Biofilm growth under elastic confinement. *Phys. Rev. Lett.* **128**, 178102 (2022).
74. R. Rusconi, S. Lecuyer, L. Guglielmini, H. A. Stone, Laminar flow around corners triggers the formation of biofilm streamers. *J. R. Soc. Interface* **7**, 1293–1299 (2010).
75. Q. Zhang *et al.*, Morphogenesis and cell ordering in confined bacterial biofilms. *Proc. Natl. Acad. Sci. U.S.A.* **118**, e2107107118 (2021).
76. G. A. Stooke-Vaughan, O. Campàs, Physical control of tissue morphogenesis across scales. *Curr. Opin. Genet. Dev.* **51**, 111–119 (2018).
77. K. Goodwin, C. M. Nelson, Mechanics of development. *Dev. Cell* **56**, 240–250 (2021).
78. D. Wirtz, K. Konstantopoulos, P. C. Pearson, The physics of cancer: The role of physical interactions and mechanical forces in metastasis. *Nat. Rev. Cancer* **11**, 512–522 (2011).
79. A. M. Jimenez Valencia *et al.*, Collective cancer cell invasion induced by coordinated contractile stresses. *Oncotarget* **6**, 43438–43451 (2015).
80. C. D. Paul, W. C. Hung, D. Wirtz, K. Konstantopoulos, Engineered models of confined cell migration. *Annu. Rev. Biomed. Eng.* **18**, 159–180 (2016).
81. H. Ahmadzadeh *et al.*, Modeling the two-way feedback between contractility and matrix realignment reveals a nonlinear mode of cancer cell invasion. *Proc. Natl. Acad. Sci. U.S.A.* **114**, E1617–E1626 (2017).
82. P. H. Wu, D. M. Gilkes, D. Wirtz, The biophysics of 3D cell migration. *Annu. Rev. Biophys.* **47**, 549–567 (2018).
83. J. N. Wilking, T. E. Angelini, A. Seminara, M. P. Brenner, D. A. Weitz, Biofilms as complex fluids. *MRS Bull.* **36**, 385–391 (2011).
84. M. Schaffner, P. A. Rühs, F. Coulter, S. Kilcher, A. R. Studart, 3D printing of bacteria into functional complex materials. *Sci. Adv.* **3**, eaao6804 (2017).
85. T. Bhattacharjee *et al.*, Writing in the granular gel medium. *Sci. Adv.* **1**, e1500655 (2015).
86. T. Bhattacharjee *et al.*, Polyelectrolyte scaling laws for microgel yielding near jamming. *Soft Matter* **14**, 1559–1570 (2018).
87. T. Bhattacharjee, S. S. Datta, Bacterial hopping and trapping in porous media. *Nat. Commun.* **10**, 2075 (2019).
88. T. Bhattacharjee, S. S. Datta, Confinement and activity regulate bacterial motion in porous media. *Soft Matter* **15**, 9920–9930 (2019).
89. A. L. Barabási, H. E. Stanley, *Fractal Concepts in Surface Growth* (Cambridge University Press, 1995).
90. M. Kardar, G. Parisi, Y. C. Zhang, Dynamic scaling of growing interfaces. *Phys. Rev. Lett.* **56**, 889–892 (1986).
91. J. A. Bonachela, C. D. Nadell, J. B. Xavier, S. A. Levin, Universality in bacterial colonies. *J. Stat. Phys.* **144**, 303–315 (2011).
92. C. D. Nadell *et al.*, Cutting through the complexity of cell collectives. *Proc. Biol. Sci.* **280**, 20122770 (2013).
93. E. Young, G. Melaugh, R. J. Allen, Pinning transition in biofilm structure driven by active layer dynamics. *bioRxiv* [Preprint] (2022). <https://www.biorxiv.org/content/10.1101/2022.03.21.485164v1> (Accessed 22 March 2020).
94. C. Blanch-Mercader, J. Casademunt, Spontaneous motility of actin lamellar fragments. *Phys. Rev. Lett.* **110**, 078102 (2013).
95. M. J. Bogdan, T. Savin, Fingering instabilities in tissue invasion: An active fluid model. *R. Soc. Open Sci.* **5**, 181579 (2018).
96. A. Mongera *et al.*, A fluid-to-solid jamming transition underlies vertebrate body axis elongation. *Nature* **561**, 401–405 (2018).
97. S. P. Banavar *et al.*, Mechanical control of tissue shape and morphogenetic flows during vertebrate body axis elongation. *Sci. Rep.* **11**, 8591 (2021).
98. Y. Guo, M. Nitzan, M. P. Brenner, Programming cell growth into different cluster shapes using diffusible signals. *PLoS Comput. Biol.* **17**, e1009576 (2021).
99. J. Li, S. K. Schnyder, M. S. Turner, R. Yamamoto, Role of the cell cycle in collective cell dynamics. *Phys. Rev. X* **11**, 031025 (2021).
100. M. Martin, T. Risler, Viscocapillary instability in cellular spheroids. *New J. Phys.* **23**, 033032 (2021).
101. L. Michaelis *et al.*, Die kinetik der invertinwirkung. *Biochem. Z.* **49**, 352 (1913).
102. L. Michaelis, M. L. Menten, K. A. Johnson, R. S. Goody, The original Michaelis constant: Translation of the 1913 Michaelis-Menten paper. *Biochemistry* **50**, 8264–8269 (2011).
103. T. Vicsek, M. Cserzé, V. K. Horváth, Self-affine growth of bacterial colonies. *Physica A* **167**, 315–321 (1990).
104. S. N. Santalla, S. C. Ferreira, Eden model with nonlocal growth rules and kinetic roughening in biological systems. *Phys. Rev. E* **98**, 022405 (2018).
105. S. N. Santalla *et al.*, Nonuniversality of front fluctuations for compact colonies of nonmotile bacteria. *Phys. Rev. E* **98**, 012407 (2018).
106. T. R. Thomas, *Rough Surfaces* (Longman, London, United Kingdom, 1982).
107. F. Family, T. Vicsek, Scaling of the active zone in the eden process on percolation networks and the ballistic deposition model. *J. Phys. A Math. Theor.* **18**, L75 (1985).
108. F. Family, Scaling of rough surfaces: Effects of surface diffusion. *J. Phys. A Math. Theor.* **19**, L441 (1986).
109. M. A. Rubio, C. A. Edwards, A. Dougherty, J. P. Gollub, Self-affine fractal interfaces from immiscible displacement in porous media. *Phys. Rev. Lett.* **63**, 1685–1688 (1989).
110. V. K. Horváth, F. Family, T. Vicsek, Dynamic scaling of the interface in two-phase viscous flows in porous media. *J. Phys. A Math. Theor.* **24**, L25 (1991).
111. S. V. Buldyrev *et al.*, Anomalous interface roughening in porous media: Experiment and model. *Phys. Rev. A* **45**, R8313–R8316 (1992).
112. S. He, G. L. Kahanda, Pz. Wong, Roughness of wetting fluid invasion fronts in porous media. *Phys. Rev. Lett.* **69**, 3731–3734 (1992).
113. J. Zhang, Y. C. Zhang, P. Alstrom, M. Levinsen, Modeling forest fire by a paper-burning experiment, a realization of the interface growth mechanism. *Physica A* **189**, 383–389 (1992).
114. T. Halpin-Healy, Y. C. Zhang, Kinetic roughening phenomena, stochastic growth, directed polymers and all that. Aspects of multidisciplinary statistical mechanics. *Phys. Rep.* **254**, 215–414 (1995).
115. R. Cuerno, A. L. Barabási, Dynamic scaling of ion-sputtered surfaces. *Phys. Rev. Lett.* **74**, 4746–4749 (1995).
116. J. Krug, Origins of scale invariance in growth processes. *Adv. Phys.* **46**, 139–282 (1997).
117. J. Soriano, J. J. Ramasco, M. A. Rodríguez, A. Hernández-Machado, J. Ortín, Anomalous roughening of Hele-Shaw flows with quenched disorder. *Phys. Rev. Lett.* **89**, 026102 (2002).
118. R. M. Sutherland, Cell and environment interactions in tumor microregions: The multicell spheroid model. *Science* **240**, 177–184 (1988).
119. J. Soriano *et al.*, Anomalous roughening of viscous fluid fronts in spontaneous imbibition. *Phys. Rev. Lett.* **95**, 104501 (2005).
120. A. Birovlev *et al.*, Gravity invasion percolation in two dimensions: Experiment and simulation. *Phys. Rev. Lett.* **67**, 584–587 (1991).
121. L. H. Tang, H. Leschhorn, Pinning by directed percolation. *Phys. Rev. A* **45**, R8309–R8312 (1992).
122. L. H. Tang, M. Kardar, D. Dhar, Driven depinning in anisotropic media. *Phys. Rev. Lett.* **74**, 920–923 (1995).
123. G. Parisi, On surface growth in random media. *Europhys. Lett.* **17**, 673 (1992).
124. J. M. López, M. A. Rodríguez, R. Cuerno, Superroughening versus intrinsic anomalous scaling of surfaces. *Phys. Rev. E Stat. Phys. Plasmas Fluids Relat. Interdiscip. Topics* **56**, 3993 (1997).
125. J. M. López, Scaling approach to calculate critical exponents in anomalous surface roughening. *Phys. Rev. Lett.* **83**, 4594 (1999).
126. J. J. Ramasco, J. M. López, M. A. Rodríguez, Generic dynamic scaling in kinetic roughening. *Phys. Rev. Lett.* **84**, 2199–2202 (2000).
127. U. Böckelmann, W. Manz, T. R. Neub, U. Szewzyka, Characterization of the microbial community of lotic organic aggregates ('river snow') in the Elbe River of Germany by cultivation and molecular methods. *FEMS Microbiol. Ecol.* **33**, 157–170 (2000).
128. K. Busch *et al.*, Bacterial colonization and vertical distribution of marine gel particles (TEP and CSP) in the Arctic Fram Strait. *Front. Mar. Sci.* **4**, 166 (2017).
129. B. Zänker, A. Engel, M. Cunliffe, Bacterial communities associated with individual transparent exopolymers particles (TEP). *J. Plankton Res.* **41**, 561–565 (2019).
130. D. A. Rosen, T. M. Hooton, W. E. Stamm, P. A. Humphrey, S. J. Hultgren, Detection of intracellular bacterial communities in human urinary tract infection. *PLoS Med.* **4**, e329 (2007).
131. E. Szabó *et al.*, Microbial population dynamics and ecosystem functions of anoxic/aerobic granular sludge in sequencing batch reactors operated at different organic loading rates. *Front. Microbiol.* **8**, 770 (2017).
132. B. M. Wilén, B. Jin, P. Lant, Impacts of structural characteristics on activated sludge floc stability. *Water Res.* **37**, 3632–3645 (2003).
133. B. Bottura, L. M. Rooney, P. A. Hoskisson, G. McConnell, Intra-colony channel morphology in *Escherichia coli* biofilms is governed by nutrient availability and substrate stiffness. *Biofilm* **100084**, (2022).
134. A. Prindle *et al.*, Ion channels enable electrical communication in bacterial communities. *Nature* **527**, 59–63 (2015).
135. J. Liu *et al.*, Metabolic co-dependence gives rise to collective oscillations within biofilms. *Nature* **523**, 550–554 (2015).
136. J. Humphries *et al.*, Species-independent attraction to biofilms through electrical signaling. *Cell* **168**, 200–209.e12 (2017).
137. J. Liu *et al.*, Coupling between distant biofilms and emergence of nutrient time-sharing. *Science* **356**, 638–642 (2017).
138. J. W. Larkin *et al.*, Signal percolation within a bacterial community. *Cell Syst.* **7**, 137–145.e3 (2018).
139. R. Martínez-Corral, J. Liu, G. M. Stiel, J. García-Ojalvo, Bistable emergence of oscillations in growing *Bacillus subtilis* biofilms. *Proc. Natl. Acad. Sci. U.S.A.* **115**, E8333–E8340 (2018).
140. J. A. Schwartzman *et al.*, Bacterial growth in multicellular aggregates leads to the emergence of complex lifecycles. *Curr. Biol.* **32**, 3059–3069.e7 (2022).
141. K. Tong, G. O. Bozdag, W. C. Ratcliff, Selective drivers of simple multicellularity. *Curr. Opin. Microbiol.* **67**, 102141 (2022).
142. A. Bonforti, R. Sole, Unicellular-multicellular evolutionary branching driven by resource limitations. *J. R. Soc. Interface* **19**, 20220018 (2022).
143. W. C. Ratcliff, R. Denison, M. Borrello, M. Travissano, Experimental evolution of multicellularity. *Proc. Natl. Acad. Sci. U.S.A.* **109**, 1595–1600 (2012).
144. S. Jacobeen *et al.*, Cellular packing, mechanical stress and the evolution of multicellularity. *Nat. Phys.* **14**, 286–290 (2018).
145. S. Jacobeen *et al.*, Geometry, packing, and evolutionary paths to increased multicellular size. *Phys. Rev. E* **97**, 050401 (2018).
146. S. A. Zamani-Dahaj *et al.*, Spontaneous emergence of multicellular heritability. *bioRxiv* [Preprint] (2021). <https://www.biorxiv.org/content/10.1101/2021.07.19.452990v2> (Accessed 20 July 2021).
147. T. C. Day *et al.*, Cellular organization in lab-evolved and extant multicellular species obeys a maximum entropy law. *eLife* **11**, e7207 (2022).
148. A. Martínez-Calvo *et al.*, Data for "Morphological instability and roughening of growing 3D bacterial colonies." Zenodo. <https://zenodo.org/record/7141219>. Deposited 3 October 2022.